Fatigue strength and life assessment of L-PBF 316L stainless steel showing process and corrosion related defects

Pierre Merot [a,b,*], Franck Morel [a], Etienne Pessard [a], Linamaria Gallegos Mayorga [a], Paul Buttin [b], Thierry Baffie [c]

[a] *Arts et Métiers Institute of Technology, LAMPA, HESAM Université, F-49035 Angers, France*
[b] *CEA, CTREG, DGDO, Bouguenais, France*
[c] *CEA-LITEN, Univ.Grenoble Alpes, Grenoble, France*

Keywords:
316L Stainless steel
Laser Powder Ded Fusion (L-PBF)
High Cycle Fatigue (HCF)
Short crack propagation
Modelization

A B S T R A C T

The present work focuses on the modelling of the fatigue behaviour of a 316L produced by laser powder bed fusion containing various defect populations : Lacks of fusion, corrosion pits and one electric discharge machined hemispherical defect. As shown in previous experimental studies, the crack leading up to failure systematically initiated on a single surface defect. The nature and morphology of the critical defect did not show any influence on the fatigue strength, and only its size seemed to matter. To take into account the critical defect size, models based on linear elastic fracture mechanics were implemented and identified. A modified Paris propagation law was used to model the short crack regime. This approach was used to predict S–N curve domains based on critical defects size range.

1. Introduction

In spite of the numerous academic papers tackling the fatigue behaviour of Additively Manufactured (AM) materials [1–3], progress on the understanding on the role played by defects related either to the fabrication process or the in-service environment remains necessary [4–6].

Regarding the Laser Powder Bed Fusion (L-PBF) austenitic stainless steel 316L, several experimental studies have shown a microstructure specific to the AM process recognizable by three characteristic markers : (i) the presence of heterogeneous grains, both in terms of size and morphology [7–9], (ii) the epitaxy phenomena, caused by powder layer superposition and the microstructure below the melt pool, which explains the presence of grains crossing several powder layers and the texture of the material [10–12], and (iii) the presence of solidification cells inside the grains, with a size near 500 nm [8,13,14]. This last feature is linked to the very high cooling rate (10^5 - 10^7 K/s) [2,15] creating a large number of dislocations on the cell walls. The presence of these dislocations has been pointed out in the literature as a potential origin of the as-built material high yield stress [1,16,17].

The complexity of the resulting microstructure coupled with the localized nature of the fatigue damage phenomenon is often proposed as an explanation to its stochastic nature. In case of AM materials, the fatigue data scatter is explained in some studies from the point of view of the spatial and defect size distributions present in the samples [18–20]. For the 316L L-PBF, fatigue behaviour seems to be affected by the presence of process related defects such as gas pores and Lack of Fusion pores (LoF) [21–23].

As pointed out by several authors [21,24,25], alloys manufactured by AM are characterized by S–N data showing a large scatter in fatigue lives and fatigue strength. This dispersion is shown in Fig. 1 and can be attributed to different sized defects at the origin of fatigue fracture and to the variation of the local microstructure at the initiation site [25–27].

* Corresponding author.
E-mail address: pierre.merot@ensam.eu (P. Merot).

https://doi.org/10.1016/j.engfracmech.2022.108883

Nomenclature

a, a_f	Crack length and critical crack size (failure) (m)
a_{trans}	Crack transition length between short and long crack regime (m)
a_0	El-Haddad's fictitious length scale (m)
C^*, m	Adapted Paris materials parameters (–)
d	Chapetti's fictitious microstructural barrier characteristic length (m)
$\delta\sigma_{max}$	Increment of the maximal nominal stress between steps (MPa)
ΔK, ΔK_{th}	Stress Intensity Factor (SIF) and its threshold (MPa $\sqrt{\text{m}}$)
$\Delta K_{th,int}$, $\Delta K_{th,ext}$	SIF intrinsic and extrinsic Chapetti's thresholds (MPa $\sqrt{\text{m}}$)
$\Delta K_{th,ext,tot}$	Total extrinsic Chapetti's SIF thresholds (MPa $\sqrt{\text{m}}$)
$\Delta\sigma$, $\Delta\sigma_{th}$	Stress range and its threshold (MPa)
$\Delta\sigma_{th,0}$	Stress range threshold of the material matrix (MPa)
σ_a, $\sigma_{a,th}$	Stress amplitude and its threshold (MPa)
σ_{max}, $\sigma_{max,th}$	Maximal stress and its threshold (MPa)
f	Crack geometric correction factor (–)
g, β	Murakami location factor and stress ratio exponent (–)
HV	Vickers Hardness (kgf/mm^2)
k	Extrinsic Chapetti's SIF thresholds exponent (–)
N, N_{ref}	Number of cycles and its reference (to define fatigue strength) (–)
R	Stress ratio ($R = \sigma_{min}/\sigma_{max}$) (–)
$\sqrt{area}$	Square root of projected area of the defect (m)
ϕ	Fatigue specimen diameter (m)

Acronyms

BD	Building Direction
EBSD	Electron BackScattered Diffraction
EDM	Electric Discharge Machining
LEFM	Linear Elastic Fracture Mechanics
LoF	Lack of Fusion
SEM	Scanning Electron Microscope
SIF	Stress Intensity Factor

In general, the largest defect contained in the loaded sample and close to the free surface is likely to be the critical defect responsible for the final failure in High Cycle Fatigue (HCF) [28,29]. Hence, assuming the defect content caused by the manufacturing process is accurately known, the fatigue response at the macroscopic scale should, in principle, be predicted from the defect population features (size, shape, position, ...) for a given microstructure.

In the High Cycle Fatigue regime for metallic materials, the major part of the total lifetime is considered to be crack initiation [31–33]. This includes all the events taking place before a crack can be considered observable (at around 1 mm) and comprises cyclic micro-plasticity, micro-crack nucleation and short crack growth [32,34]. For metallic alloys, the term "short crack" refers in general to a crack with a length in the order of magnitude of a few grains [35]. In this cracking regime, local plasticity within grains is the main phenomenon governing crack growth [22,36]. When the crack becomes larger than a given critical size (related to the microstructure), a transition between crack initiation and crack propagation occurs. The microstructure features become small compared to the crack size and the crack propagation is dominated by the general microstructure state instead of the local one. This is referred to as long crack behaviour [37–39].

In order to predict long crack behaviour, Linear Elastic Fracture Mechanics (LEFM) can be applied [40,41]. However, short fatigue cracks growth cannot be modelled using this theory alone, since LEFM leads to non-conservative predictions [42–44]. Indeed, examples in the literature showed crack propagation at stresses below the long crack propagation threshold [40,45,46]. A lot of different LEFM based models were proposed to consider the particular short crack problem [36,47,48]. Among these approaches, several authors suggested to make the crack propagation threshold depends on the crack size [35,49,50]. Experimental evidences support this dependency, which was explained by some researchers by the progressive activation of crack closure mechanisms as the crack propagates [42,51]. This approach was adopted in this paper through the implementation of size dependent threshold's models from the literature.

The aim of this study is to make use of LEFM to model defects in an AM material (316L L-PBF) in the hopes of gaining some insight on the HCF performance of this type of alloys. The purpose is twofold. First, to bring complements to the experimental study described in a previous paper [30]. In particular, a comparison with a wrought 316L steel is carried out to distinguish the

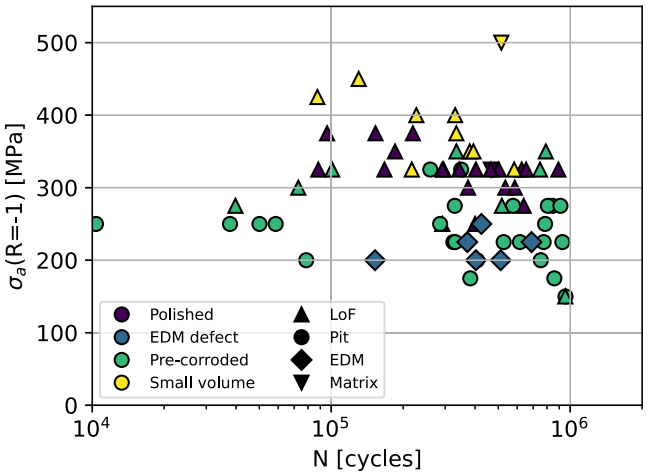

Fig. 1. SN curves in air for $R = -1$ of different batches with crack initiation on various defect types. The batch is represented by the colour of the point, the killer defect type by its marker shape. A part of the data was published in a previous paper [30].

respective roles of the microstructure and the defects. Three types of defects are studied : LoF, Corrosion Pits and EDM hemispherical defects. Second, to test several short crack growth models and compare their predictions to the experimental data collected from the comprehensive fatigue campaign on this AM 316L austenitic stainless steel. For the smallest defects, the dependency of the threshold stress intensity factor to the defect size is investigated by means of three classic models from the literature. The consideration of such size dependency leads to more conservative predictions, particularly in the short-crack regime. The issue of fatigue lives scatter is also emphasized from the point of view of defects.

2. Material and experiments

2.1. Preparation of fatigue tested samples

In this study, the material used is a 316L grade stainless steel manufactured by L-PBF. The alloy was received as a powder and provided by TLS Technik. Fatigue specimens were vertically built under a Nitrogen (N) atmosphere by a Farsoon FS271M L-PBF machine. A laser power of 225 W, with a laser scan speed of 1000 mm/s and a layer thickness of 30 µm were used. A rotation of 67° of the scan pattern was performed between each layer. A detailed description of the powder and the L-PBF process parameters can be found in a previous paper [30].

Once the L-PBF process finished, samples were detached from the plate and machined. Thus, solely the inner volume of the material was characterized. Each specimen was manually polished to avoid machining artefacts. Fig. 2 shows the two specimen geometries used in the experimental campaign.

To understand the reasoning behind the use of these two geometries, the notion of Highly Stressed Volume (HSV) needs to be introduced. In the context of our study, the HSV was defined, by means of a finite element approach, as the volume of the specimen where the von Mises stress was greater than 90% of the von Mises maximal stress calculated for the entire specimen. The geometry shown in Fig. 2(a) has an HSV of 1005 mm^3, the geometry in Fig. 2(b) has an HSV of 8 mm^3. As the HSV decreases, the chances of the failure inducing being on the larger side of the defect size distribution will also diminish. This HSV modification strategy has been used successfully to observe the impact of small defects on the fatigue behaviour of other AM specimens [25,52], but also for casted [18] and machined [53] aluminium alloys.

To observe the sensitivity of the material to different types of defects, four batches were prepared from the original machined then polished specimens: (i) without any supplementary operation “polished” (17/65), (ii) pre-corroded by anodic polarization “pre-corroded” (32/65), (iii) with an EDM hemispherical defect “EDM defect” (6/65) and (iv) machined and polished as to reach the small volume geometry “small volume” (10/65). Fig. 3 represents the different steps of the fabrication of the different tested batches.

2.2. Material microstructure

In order to observe the microstructure of the bulk material, a planar sample was polished and chemically etched using a colloidal silica suspension (SiO_2). Electron BackScattered Diffraction (EBSD) analyses were then conducted. The grain detection criterion was set to 5° in terms of misorientation from a pixel to another. Data was taken from Guerchais’ works [54] for a wrought 316L for comparison purposes. Fig. 4 presents the qualitative EBSD grain cartography. In this representation, different colours were used to clearly separate grains and do not correspond to any texture information.

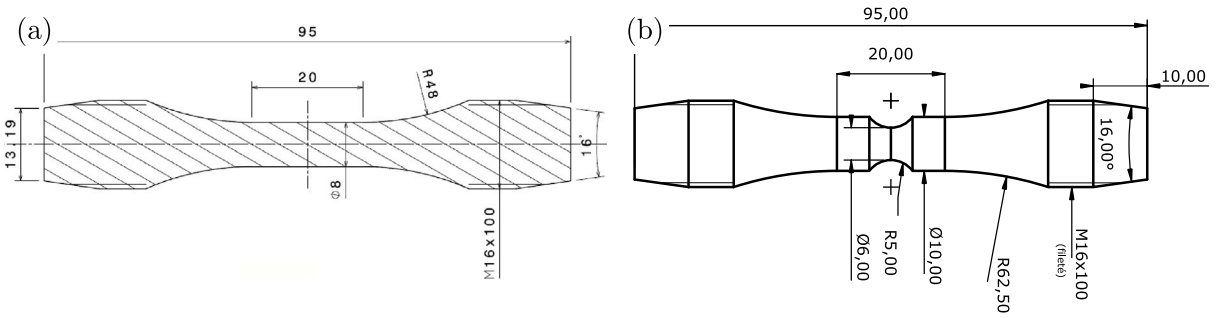

Fig. 2. Fatigue samples geometries (dimensions in mm), with (a) the reference geometry (55 specimens) and (b) the small volume geometry (10 specimens).

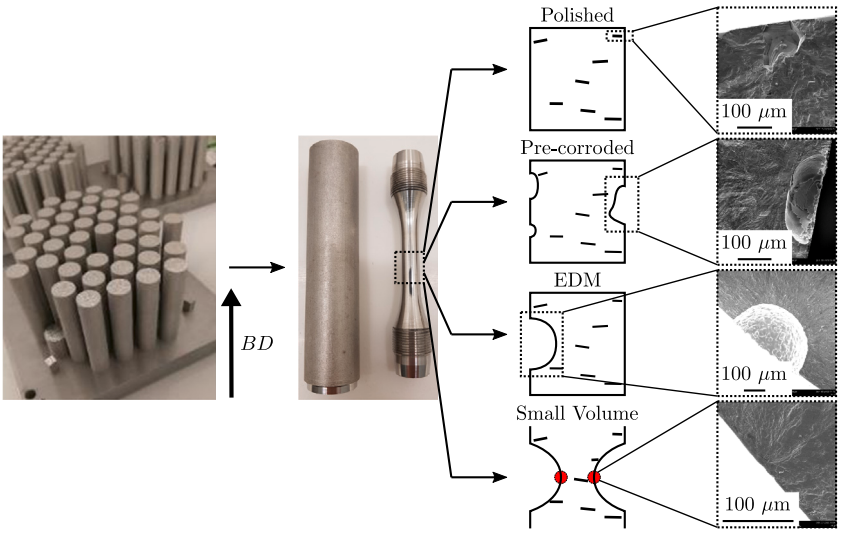

Fig. 3. Different steps of the fabrication of the different tested batches. The SEM fractographies show a LoF, a corrosion pit, a hemispherical EDM defect and a metallic matrix initiation.

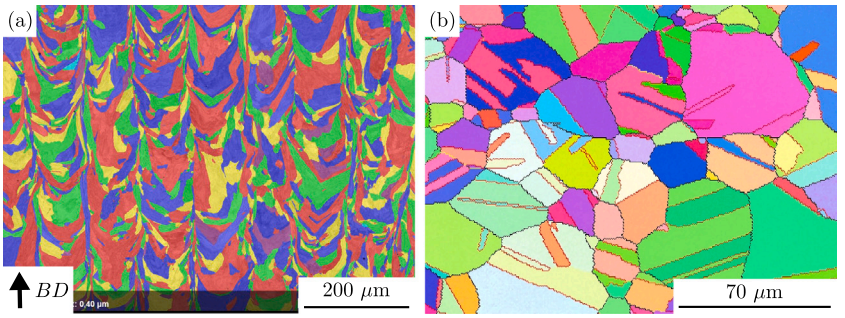

Fig. 4. Qualitative EBSD grains identification on 316L (a) L-PBF and (b) wrought [54].

Depending on the manufacture process, the materials present different microstructures. The mean grain size values, for grain maps shown in Fig. 4, were found equal to 49 μm and 11 μm for the L-PBF and wrought material respectively. The mean value was more than four times smaller for the wrought 316L than for the L-PBF one. The standard deviation was equal to 30 μm for the L-PBF and 7 μm for the wrought one. Then, its value was also around four times bigger for the L-PBF material than for the wrought. Altogether, observations showed a more homogeneous grain population in terms of size for the wrought 316L when compared with the L-PBF one.

This higher homogeneity is also observable in terms of grain morphology, the wrought material showed principally equiaxed grains. In contrast, the L-PBF material was composed of a mix of equiaxed, elongated and “U” shaped grains. Equiaxed grains were

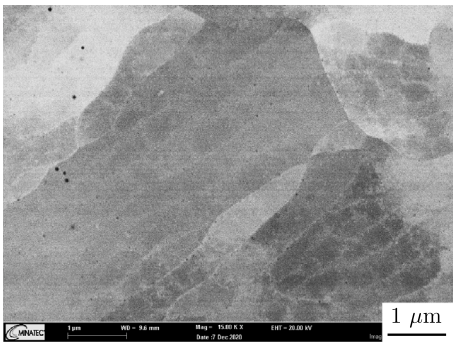

Fig. 5. Solidification cells in 316L L-PBF.

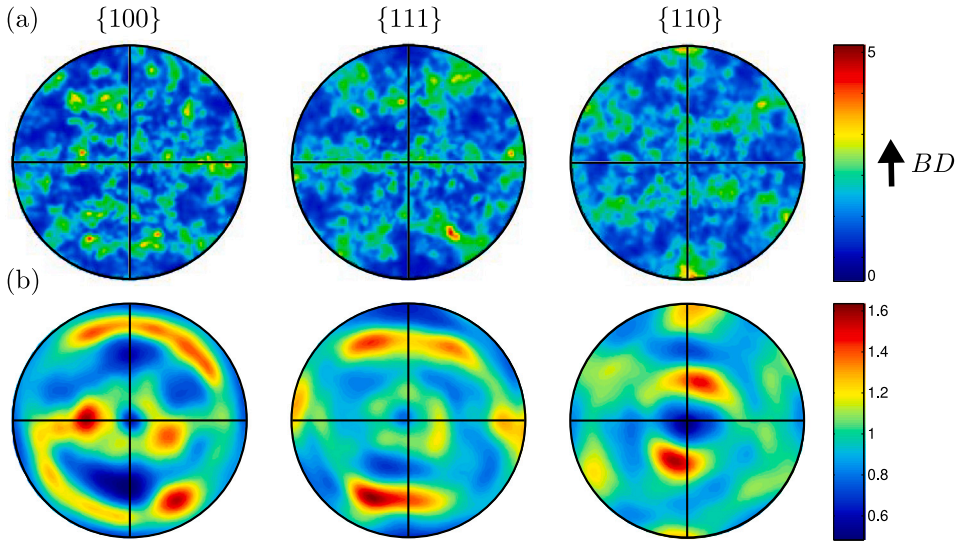

Fig. 6. EBSD pole figures on 316L (a) L-PBF and (b) wrought [54].

smaller than the other two populations. As described by Andreau et al. [10], this heterogeneity is due to different solidification mechanisms, and more specifically, to the competition between the thermal gradient direction and the epitaxy phenomena [55,56].

Furthermore, solidification cells were noticed in the grains of the L-PBF material (see Fig. 5). This feature appears as a consequence of high cooling rates (5×10^5 - 4×10^7 K/s) observed in L-PBF processes [15,57] for this type of alloy. The size of these features was found close to 500 nm, which is in good agreement with the literature [4,58,59]. It worth noting that a large number of dislocations were observed on the cells walls by several authors [60–62]. These dislocations could affect the mechanical behaviour of the material [63].

The texture of both materials (L-PBF and wrought) was also characterized. Fig. 6 represents pole figures for both materials. We notice a texture three times more pronounced for the L-PBF. <110> parallelly to the BD was the main texture of the additively manufactured material, which is consistent with observations found in the literature [64,65]. Again, the epitaxy of the grains is the principal factor driving the texture of the 316L L-PBF.

2.3. Quasi-static tests

The static behaviour was investigated by carrying tensile tests and Vickers hardness (HV) measurements on our L-PBF specimens. For comparison purposes, heat-treated specimens (1050 °C for 30 min under vacuum, N2–H2 quenching under 3–4 bar) were also tested. Four tensile tests were carried out on as-built specimens and three on heat-treated ones. Tensile specimens were vertically built (*i.e.* load axis parallel to BD). The Vickers hardness was measured under a 20 kg load. At least ten indentations were performed per type of specimen. The mean values of the obtained static behaviour were then computed. The results of these characterizations are summarized in the Table 1.

For the as-built material, our results are in good agreement with Andreau's observations [64]. It seems that the heat treated 316L L-PBF static behaviour is similar to the wrought one [54]. The heat-treatment seems to decrease the yield stress (YS) of the

Table 1
Tensile tests and hardness results for as-built and heat-treated L-PBF 316L compared to wrought 316L [54] and Andreau's data [64].

Batch	UTS (MPa)	YS (MPa)	El.% (%)	HV (–)
As-built	642	484	67	225
As-built [64]	583	448	54	236
Heat-treated	626	377	71	194
Wrought [54]	644	346	60	189

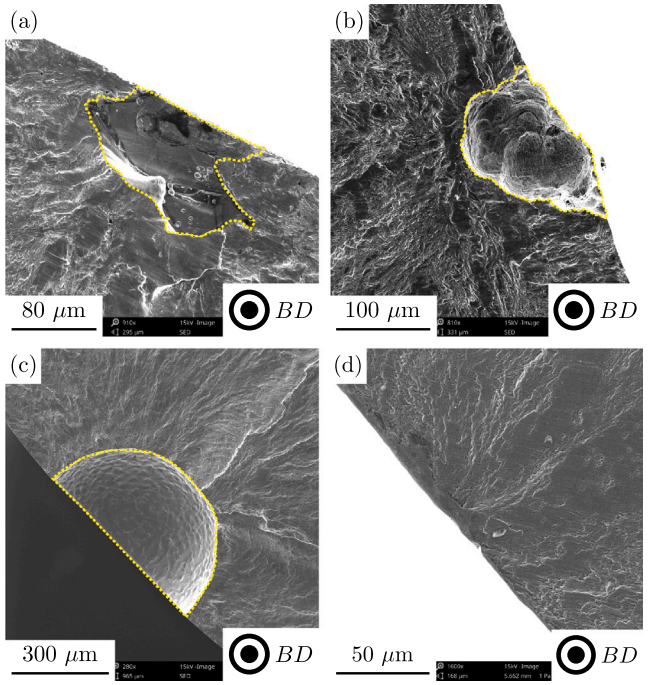

Fig. 7. SEM observations of cracks initiations from (a) a LoF defect, (b) a corrosion pit, (c) an EDM hemispherical defect and (d) the metallic matrix.

316L L-PBF by more than 100 MPa. The Vickers hardness was also negatively altered by the heat treatment, decreasing its value of 15%.

In the literature, Hlinka et al. [66] observed that with a similar heat-treatment, a total recrystallization of the microstructure occurred. The lower HV and YS after heat-treatment could probably be explained by the coarsening of the material grains and the disappearance of the solidification cells saturated in dislocations [2,15,26].

2.4. Fatigue test methodology

Uniaxial fatigue tests were carried out on a MTS Landmark 100 kN servohydraulic fatigue test machine, in air and at room temperature (≈ 20 °C). Tests were conducted using load control mode. 62 specimens vertically built were tested under fully alternative loads ($R = -1$), at a frequency of 15 Hz. Only 3 fatigue tests were carried out under $R = 0.1$ at 25 Hz. A step by step method was used, with $\Delta N = 10^6$ cycles per step as described by Maxwell and Nicholas [67]. Fatigue tests were carried out till fracture (50% displacement drift) of the specimen. All our experimental data were published and are available online [68]. This study focuses on only a part of these data.

2.5. Fracture surface analysis

After the fatigue tests, each fracture surface was observed using a Phenom XL Scanning Electron Microscope (SEM). Cracks were observed to initiate on different types of defects: (i) LoF (33/65), (ii) corrosion pits (25/65) or (iii) EDM defect (6/65). Examples of these three types of defect at the origin of the crack initiation are shown in Fig. 7(a)(b)(c). For the "pre-corroded" batch, 25 cracks initiated on corrosion pits and 7 on LoF defects. A competition between these defects of different natures was observed. For one specimen from the "small volume" batch, no defect was observed at the crack initiation site (see Fig. 7(d)). The crack initiation origin was attributed in this case to the metallic matrix of the material.

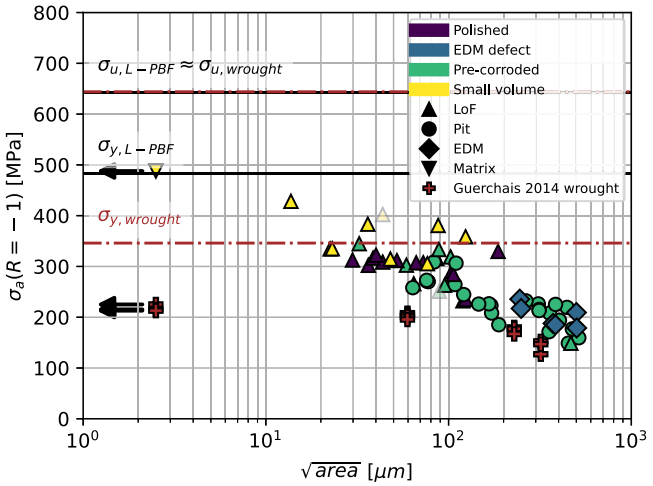

Fig. 8. Kitagawa–Takahashi diagram of the corrected data (using Eq. (1)) at $N_{ref} = 10^6$ cycles. The marker colour refers to the batch belonging of the specimen, its shape to the critical defect type (e.g. a green triangle refers to a pre-corroded specimen with a crack initiation on a LoF defect). Marker was set in transparency if the specimen broke at the first step and below 10^5 cycles. If no critical defect was observed, the metallic matrix was considered as the origin of the crack initiation. As no defect size could be measured, the $\sqrt{area}$ is arbitrary defined and a black arrow meaning that the true defect size is smaller was plotted.

2.6. Effect of the defect size

Following the convention of size description of defects by the square root of their projected area on a plane perpendicular to the loading direction [69], defect size on our specimens was calculated as the mean value of the defect size measured on the two fracture surfaces. In order to estimate the fatigue strength at $N_{ref} = 10^6$ cycles (corresponding to the HCF domain), Maxwell and Nicholas correction was used [67]. Eq. (1) defines the fatigue maximal stress threshold (or fatigue strength) $\sigma_{max,th}$, the maximal stress at the step "k" is $\sigma_{max,k}$, $\delta\sigma_{max}$ is the increment of the maximal nominal stress between steps and N_k is the number of cycles at step "k".

$$\sigma_{max,th} = (\sigma_{max,k} - \delta\sigma_{max}) + \delta\sigma_{max}\left(\frac{N_k}{N_{ref}}\right) \tag{1}$$

"k" is the step when the fracture occurs, meaning that $N_k < N_{ref}$.

Fig. 8 represents the data in a Kitagawa–Takahashi diagram in terms of stress amplitude at $N_{ref} = 10^6$ cycles and square root of the area of the defect at $R = -1$. Wrought 316L data were taken from Guerchais' work [54] for comparison. The stress amplitude used was corrected using Eq. (1) for both data series. For our data, only one specimen showed a crack initiation on the material matrix ("small volume" batch). This data point is worth of mention since it gave an information about the fatigue strength of a defect-free L-PBF 316L. The observed defect-free fatigue strength (488 MPa) was found close to the yield stress of the material (484 MPa). For the wrought material (Guerchais [54]), the fatigue limit (220 MPa) was near 64% of the yield strength (346 MPa). This suggests that the metallic matrix fatigue strength might be correlated to the static behaviour – particularly the yield strength – of the 316L. The ultimate tensile stress was almost identical for L-PBF and wrought 316L (642 and 644 MPa respectively). The difference in terms of yield stress may be attributed to the high density of dislocations on the solidification cell walls [4,15,57].

Globally, a correlation between the critical defect size and the fatigue strength of the specimen could be observed. This correlation seems independent of the critical defect's nature. Its 2D projected shape did not show any influence on the fatigue strength either [30]. Since the critical defect's size appeared to be the highest relevance parameter to infer the fatigue strength, LEFM approaches which are based on the crack size could be efficient to model the effect of defects in this material. No distinction between the different defect types are made in the rest of this article.

We can notice that for small defects (below 100 μm) – or without any defect – the fatigue strength of the L-PBF alloy is higher than for the wrought material. The difference between the two materials seems to decrease when the defect size increases. Fatigue resistances are equivalent when the $\sqrt{area}$ is higher than 100 μm. We can suggest that the effect of the microstructure becomes insignificant when the defect is much bigger than microstructural features (such as grains and solidification cells in L-PBF materials). As discussed by Nadot et al. [39], the defect physical size is not as important as the relative size of the defect compared to the microstructure in which it is embedded.

In LEFM, the main driving force can be estimated by the Stress Intensity Factor (SIF) ΔK. The SIF can be calculated from Eq. (2), with f as a crack geometric correction factor equal to 0.65 for semi-circular cracks (for a surface intersecting crack) or 0.5 for internal circular cracks as suggested by Murakami [43]. $\Delta\sigma$ is the applied stress range and a is the crack length. In this paper, the crack length a is considered as the square root of the area of the crack $\sqrt{area}$.

$$\Delta K = f\Delta\sigma\sqrt{\pi a} \tag{2}$$

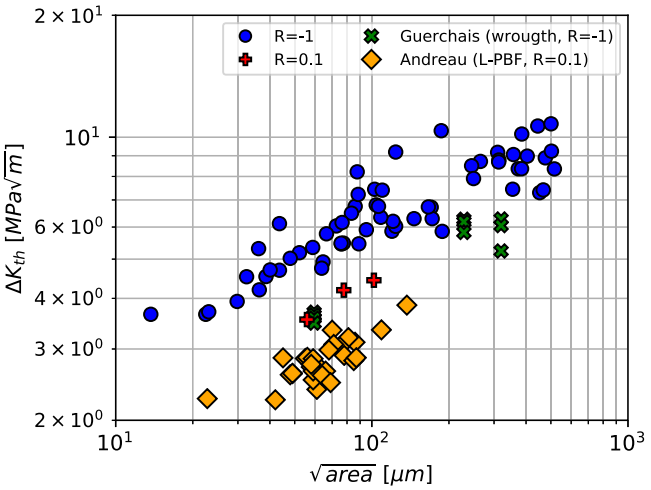

Fig. 9. ΔK_{th} as a function of the defect size $a = \sqrt{area}$. Data at $R = -1$ and $R = 0.1$ in air are compared with data of Guerchais [54] for a wrought 316L at $R = -1$ and Andreau [64] for a L-PBF 316L at $R = 0.1$.

In order to determine if the crack will propagate, the SIF have to be compared to the SIF threshold ΔK_{th}. The SIF threshold ΔK_{th} can be deduced from Eq. (2), with $\Delta\sigma_{th}$ as the stress range threshold:

$$\Delta K_{th} = f\,\Delta\sigma_{th}\sqrt{\pi a} \tag{3}$$

Because we deal with HCF, we considered $\Delta\sigma_{th}$ as equal to the experimental fatigue limit in terms of stress range.

The SIF threshold ΔK_{th} was then calculated using Eq. (3). The Fig. 9 shows ΔK_{th} as a function of the defect size $\sqrt{area}$. Data taken from Andreau's study [64] on a L-PBF 316L ($R = 0.1$) and Guerchais' work [54] on a wrought 316L ($R = -1$) are also plotted. At $R = 0.1$, only three specimens were tested. Although higher values of the SIF threshold were found for our specimens in comparison to those of Andreau ($R = 0.1$), both datasets remain in good agreement.

Fig. 9 also shows that the threshold ΔK_{th} does not remain constant for the defect size range investigated here. It drops as the defect size decreases. This tendency is well known and has been observed in many studies [69–71]. The next section aims at testing several approaches to model this behaviour.

3. Crack propagation threshold models

A large number of models of crack propagation thresholds can be found in the literature. Fig. 10 gives a schematic view of a Kitagawa–Takahashi diagram using Kitagawa–Takahashi [72], Murakami [69], El-Haddad [49] and Chapetti [35] models. Differences between these models are emphasized and discussed in the following subsections.

3.1. Murakami's model

One of the well-known models in the literature to estimate the SIF threshold was proposed by Murakami and Endo [69] in 1994. This model can be described through Eq. (4):

$$\Delta K_{th} = g(HV + 120)a^{2/n}\left(\frac{1-R}{2}\right)^{\alpha} \tag{4}$$

with $g = 3.3\times10^{-3}$ for an external crack and $g = 2.77\times10^{-3}$ for an internal one. HV is the material Vickers hardness (225), $a = \sqrt{area}$ is the crack length (equal to the square root of the projected defect area) (in μm), R is the stress ratio and $\alpha = 0.226 + HV\times10^{-4}$. In the original model, $n = 6$. We can notice that α was initially proposed for hard steels and may be re-estimated for the 316L L-PBF [43,71]. According to Murakami [43], this model could be used from a few microns to a thousand of microns (depending on the material).

The upper limitation of the original Murakami's model was first introduced and explained by Chapetti [73]. He suggested that when the crack size a becomes higher than a transition size a_{trans}, ΔK_{th} remains constant and is equal to $\Delta K_{th,LC}$. Schönbauer and Mayer [71] extended this limitation and considered the transition size a_{trans} as independent of the load ratio R.

Since no information could be found in the literature to estimate the value of a_{trans} for the L-PBF 316L, we chose a value of 300 μm which seems coherent with our data. Murakami's model could be rewritten:

$$\begin{cases} \Delta K_{th} = \min\left\{ g(HV+120)a^{2/n}\left(\frac{1-R}{2}\right)^{\alpha},\ \Delta K_{th,LC} \right\} \\ \Delta K_{th,LC} = g(HV+120)a_{trans}^{2/n}\left(\frac{1-R}{2}\right)^{\alpha} \\ \alpha = \beta + HV\times10^{-4} \end{cases} \tag{5}$$

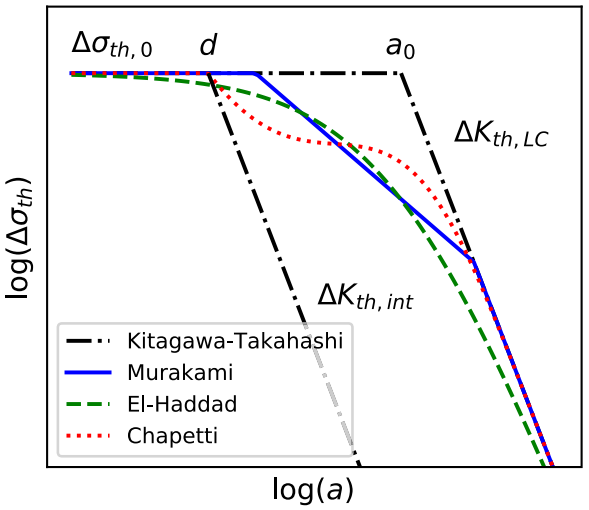

Fig. 10. Schematic Kitagawa–Takahashi diagram ($\Delta\sigma_{th}$ as a function of the crack size a) with Kitagawa–Takahashi [72], Murakami [69], El-Haddad [49] and Chapetti [35] models.

In order to improve the model's accuracy, g and β were identified using our dataset (*i.e.* fitted). It is worth noting that n was kept equal to 6 as suggested by Murakami [69]. g was identified on the $R = -1$ data and was found equal to 3.91×10^{-3}. Then, the effect of R through β was adjusted using the $R = 0.1$ data. The optimum β was found equal to 0.410 instead of the value of 0.226 proposed by Murakami and Endo [69]. The long crack threshold $\Delta K_{th,LC}$ obtained at $R = -1$ and $R = 0.1$ were found equal to 9.04 MPa $\sqrt{\text{m}}$ and 6.40 MPa $\sqrt{\text{m}}$ respectively. We can recall that Riemer and Richard [74] obtained a value of $\Delta K_{th,LC} \simeq 5$ MPa $\sqrt{\text{m}}$ for a L-PBF 316L at $R = 0.1$, which is coherent with our calculated value. The identified Murakami's model is plotted in Fig. 11(a) in terms of stress for $R = -1$ and in Fig. 11(b) in terms of SIF threshold for both stress ratios. Data description through this upgraded model (with g and β values fitted on our dataset) can be considered as satisfactory.

3.2. El-Haddad's model

Another classic model in the literature [31,75] was proposed by El Haddad et al. [49]. The SIF threshold can be written by Eq. (6), with $\Delta\sigma_{th,0}$ the stress range threshold of the material without defects.

$$\begin{cases} \Delta K_{th} = \Delta K_{th,LC}\sqrt{\frac{a}{a+a_0}} \\ a_0 = \frac{1}{\pi}\left[\frac{\Delta K_{th,LC}}{f\,\Delta\sigma_{th,0}}\right]^2 \end{cases} \tag{6}$$

The SIF threshold value increases from 0 to $\Delta K_{th,LC}$ when the crack size increases from 0 to $+\infty$. The value of $\Delta\sigma_{th,0}$ was set to 900 MPa which is consistent with our observation when cracks initiate on the metallic matrix for $R = -1$ and 511 MPa for $R = 0.1$ in accordance with Andreau's study [64]. Since $\Delta K_{th,LC}$ was identified previously with Murakami's model, El-Haddad can be used without any other identification. The El-Haddad's model is plotted in Fig. 11 and seems as consistent as Murakami's model.

3.3. Chapetti's model

In El-Haddad and Murakami's models, the SIF threshold is higher than 0 if the crack exists, even for small cracks. However, many researchers reported that crack closing phenomena are negligible for microstructurally small cracks, leading to an over-estimation of ΔK_{th} and non-conservative models [35,40,42].

To address this issue, Chapetti [35] proposed a model where the SIF threshold is defined as a sum of intrinsic ($\Delta K_{th,int}$) and extrinsic ($\Delta K_{th,ext}$) thresholds:

$$\Delta K_{th} = \Delta K_{th,int} + \Delta K_{th,ext} \qquad \forall\ a \geq d \tag{7}$$

$\Delta K_{th,int}$ represents the microstructural crack propagation resistance and is defined as:

$$\Delta K_{th,int} = f\,\Delta\sigma_{th,0}\sqrt{\pi d} \tag{8}$$

with d the microstructural barrier characteristic length. We can notice that this intrinsic SIF threshold is a constant for the material. The extrinsic SIF threshold can be written as:

$$\Delta K_{th,ext} = \Delta K_{th,ext,tot}\left\{1 - \exp\left[-k(a-d)\right]\right\} \qquad \forall\ a \geq d \tag{9}$$

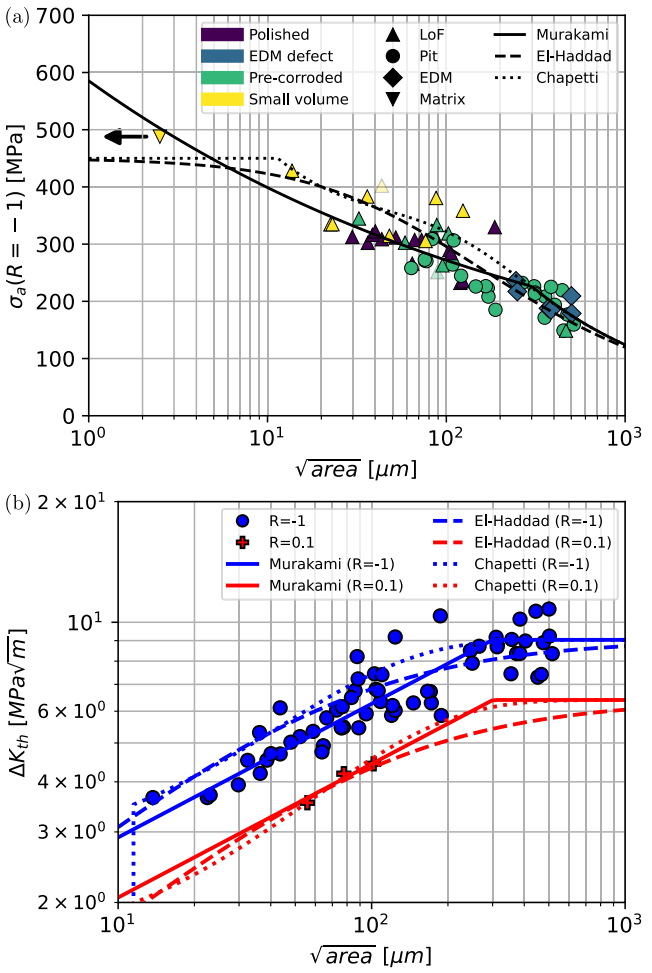

Fig. 11. (a) $\Delta\sigma_a$ as a function of the crack size a ($R = -1$) and (b) ΔK_{th} as a function of the defect size $a = \sqrt{area}$ ($R = -1$ and $R = 0.1$) in air. The fitted models' predictions (Murakami, El-Haddad and Chapetti) are also plotted.

with $\Delta K_{th,ext,tot}$, the total extrinsic SIF threshold:

$$\Delta K_{th,ext,tot} = \Delta K_{th,LC} - \Delta K_{th,int} \tag{10}$$

and k the extrinsic Chapetti's SIF thresholds exponent:

$$k = \frac{1}{4d}\frac{\Delta K_{th,int}}{\Delta K_{th,ext,tot}} \tag{11}$$

In order to fit Chapetti's model to our dataset, the parameter d was identified and found equal to 11.43 μm using a least square error minimization on the $R = -1$ data. We can notice that this value is between the mean grain size (around 45 μm) and the solidification cells size (around 500 nm). It is then possible that this characteristic length represents the effect of two types of microstructural barriers. The evolution of ΔK_{th} as a function of the crack size is plotted in Fig. 11(b). Again, this model seems representative of our experimental data.

3.4. Models comparison

The three presented fitted models are in good agreement with our dataset. Murakami's model is purely empirical while El-Haddad's and Chapetti's are based on LEFM. These latter two manage a smooth transition between short and long crack regimes. Chapetti's model can be seen as an evolution of El-Haddad's model. The main difference being that Chapetti's model also takes into account a minimal size related to the material microstructure, below which, no crack closure phenomena can occur.

In the following section, a way to embed the crack propagation threshold as a driving force of the crack growth behaviour is discussed.

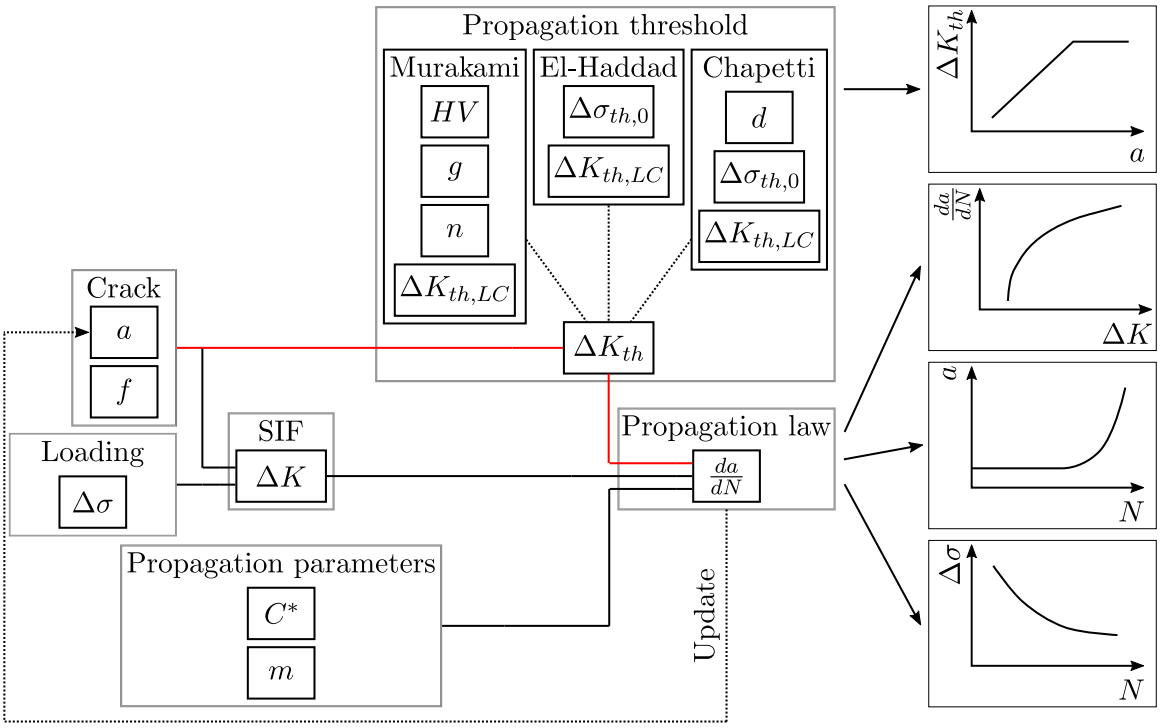

Fig. 12. Schematic representation of the propagation model with the influence of different parameters for a given loading ratio R.

4. Crack growth behaviour

In LEFM, the SIF is often considered as the main driving force of the crack propagation. The crack is considered propagating when $\Delta K > \Delta K_{th}$. For long cracks, the crack expansion size could be directly related to the SIF using the Paris law [46,76]:

$$\frac{da}{dN} = A\Delta K^b \tag{12}$$

with A and b, two materials parameters. However, this expression is no more valid in the short crack propagating regime. In the literature [31,77,78], an adapted form of the Paris law can be found in order to describe both short and long crack behaviour:

$$\frac{da}{dN} = C^*(\Delta K - \Delta K_{th})^m \tag{13}$$

with C^* and m, two materials parameters. In this equation, the SIF threshold is taken into account and the difference between ΔK and ΔK_{th} becomes the crack propagating driving force. For short cracks, ΔK and ΔK_{th} values are close which leads to a slow propagation. Since ΔK_{th} depends on R, taking the threshold into account is also a way to link the crack propagation behaviour with the applied stress ratio [32]. We chose to use $C^* = 6.25 \times 10^{-10}$ and $m = 3.94$, as determined by Riemer et al. [79] on a L-PBF 316L vertically build on CT specimens (at $R = 0.1$). It could be pointed out that no values of these parameters were found in the literature for $R = -1$. Riemer's data were then considered as an acceptable estimation for C^* and m parameters.

Fig. 12 represents schematically the crack propagation model with its different inputs. We can notice that crack parameters (a and f) are not only necessary for the computation of ΔK, but also to determine ΔK_{th}. The threshold is dependent on the crack length, which is a major difference with classic LEFM propagation models for long crack [5,80,81]. In this figure, we can clearly identify that the choice of the SIF threshold model impacts the crack propagation predictions. The schematically described iterative process is used in the rest of this article to infer the crack size as a function of the number of cycles and the applied stress range.

Fig. 13 represents the crack propagation da/dN as a function ΔK. Blue and red curves represent initial defect sizes of 20 μm and 100 μm respectively. As it can be observed on Fig. 9, the sizes of 20 and 100 μm were chosen to be representative of small and medium scale defects of the critical defect population. The stress range threshold was determined by increasing its value incrementally (step of 5 MPa) until the initial crack propagation rate reached 10^{-12} m/cycle or higher. Then, the loading imposed remained constant to predict the da/dN curve in the propagation domain.

In Fig. 13, the influence of the initial crack size on the stress threshold for different models and stress ratios can be observed. The smaller the initial crack, the higher the stress crack initiation threshold ($\Delta\sigma_{th}$) is. We can highlight that crack behaviour is different depending on the chosen threshold model as it affects the stress threshold level. The crack SIF threshold (ΔK_{th}) is smaller for smaller cracks. It means that each model is compatible with the idea that crack closing mechanisms increase when the crack

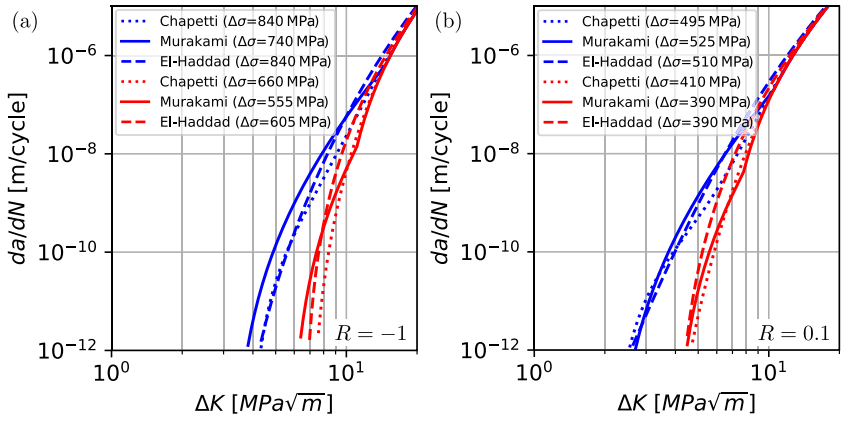

Fig. 13. Crack propagation rate da/dN as a function of the SIF ΔK for Chapetti, Murakami and El-Haddad identified models with (a) $R = -1$ and (b) $R = 0.1$. The initial crack size was set to 20 μm for the blue curves and 100 μm for the red ones. The minimal stress range to initiate the crack is written in the legend (in MPa).

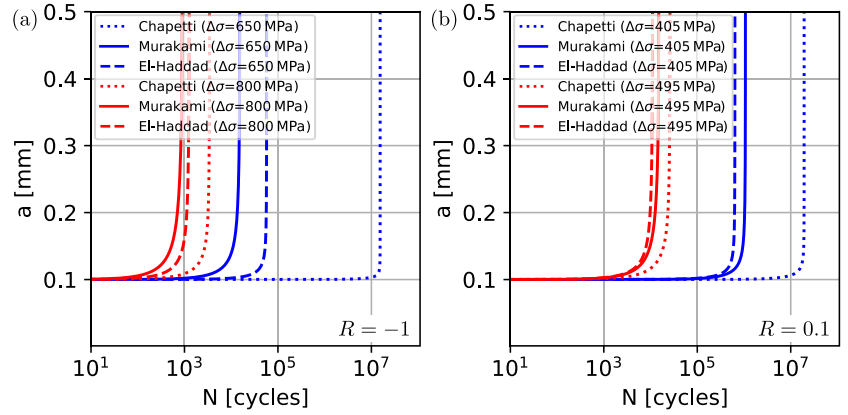

Fig. 14. Crack size growth a as a function of the number of cycles N for Chapetti, Murakami and El-Haddad identified models with (a) $R = -1$ and (b) $R = 0.1$. The initial crack size was set to 100 μm. The applied stress range was 650 MPa (blue) and 800 MPa (red) at $R = -1$ and 405 MPa (blue) and 495 MPa (red) at $R = 0.1$.

size increases. When the crack propagation becomes faster (*i.e.* long crack), the propagation behaviours become similar for both tested stress ratios. The stress range threshold is higher at $R = -1$ than at $R = 0.1$. It could be justified by the fact that for $R = -1$, a large part of the loading is compressive which is less harmful than tensile stresses that open cracks. The maximal stress is higher at $R = 0.1$ than at $R = -1$.

The Fig. 14 represents a case where the initial crack size is set equal to 100 μm for two loading conditions ($R = -1$ and $R = 0.1$). The crack behaviour is highlighted in terms of crack growth as a function of the number of cycles. We can notice that even if the crack propagation behaviours seem close in Fig. 13, the crack growth is highly affected by the choice of the SIF threshold model. This choice seems even more relevant when the loading decreases since the short crack propagation part of the total lifetime increases. A good description of the short crack behaviour is thus crucial in HCF regime.

5. Fatigue life estimation

To make a fatigue life estimation using LEFM, we should provide a failure criterion to state if the specimen is broken or not. As our experiments were conducted on fatigue specimens, we defined a critical crack size a_f by the following equation:

$$a_f = \sqrt{S/2} \qquad \text{with} \qquad S = \pi\phi^2/4 \tag{14}$$

with $\phi = 8$ mm, the fatigue specimen diameter. The specimen is considered broken when the crack surface reaches half of its initial section. Then, we considered that the failure occurred if $a > a_f$. Since the crack growth increases drastically (see Fig. 14) at the end of the sample life, the value of a_f does not need to be finely set and only its order of magnitude is of relevance.

To gain some insight on the effect of the initial crack size (*i.e.* defect size) on the fatigue lifetime, the models were used with different initial defect sizes. The Fig. 15 shows the models predictions for three defect sizes (50, 100, 200 μm) at (a) $R = -1$ and (b)

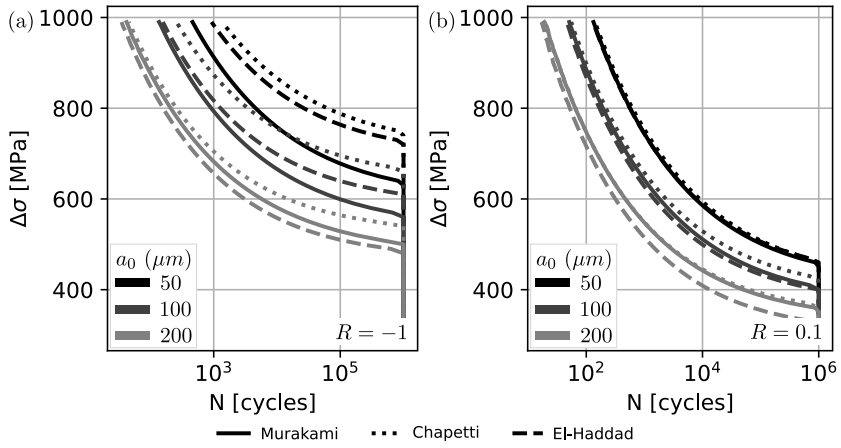

Fig. 15. Influence of the defect at the origin of crack initiation a_0 on the fatigue lifetime for Chapetti, Murakami and El-Haddad identified models with (a) $R = -1$ and (b) $R = 0.1$.

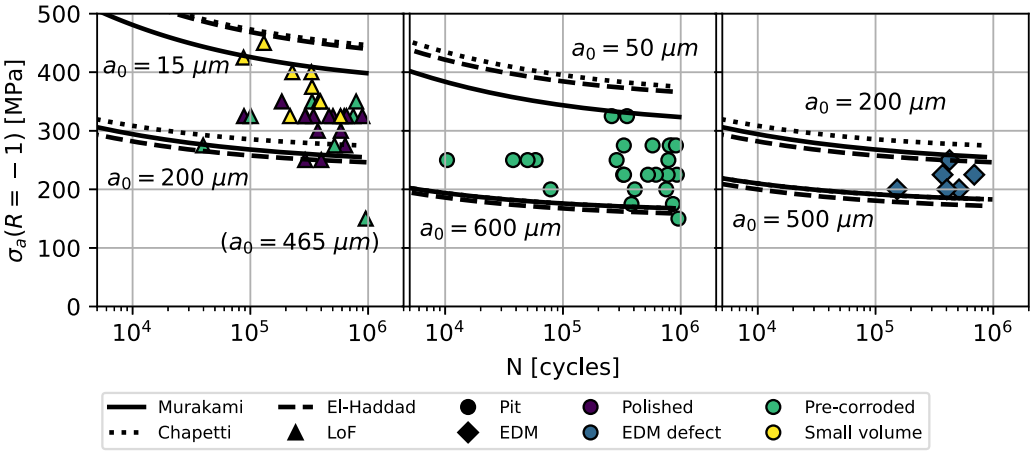

Fig. 16. Lifetime predictions for different defects sizes a_0 for Chapetti, Murakami and El-Haddad identified models at $R = -1$. Experimental data are plotted for comparison purpose. The critical defect type (LoF, corrosion pit, EDM defect) is represented by the marker shape and its batch by the marker colour. Data are separated in three graphs for each critical defect types (LoF, corrosion pit and artificial hemispherical defect respectively). The two values of a_0 chose on each subplot were fixed in order to represents lower and upper bounds in terms of size for each critical defect types.

$R = 0.1$. Predictions were obtained following the iterative process described in Fig. 12. We can observe that the fatigue resistance decreases when the defect initial size increases. Globally, the whole S–N curve seems translated down when the initial crack size increases. Differences between models increase when the stress range decreases due to a bigger fraction of the lifetime in the short crack regime.

In our previous work [30], we observed that the critical defect size was the unique morphology parameter showing a correlation with the fatigue limit of a specimen. To highlight this link between lifetime predictions and defect sizes, Fig. 16 shows lifetime predictions for different defects sizes for the three discussed models at $R = -1$. The values of the initial defect sizes were fixed in order to be representative of each population of defects: 15 to 200 μm for LoF defects, 50 to 600 μm for corrosion pits and 200 to 500 μm for EDM hemispherical defects.

For both stress ratios ($R = -1$ and $R = 0.1$), the fitted models' predictions are in good agreement with our experimental data. Indeed, LoF, corrosion pits and EDM defects lied between their respective upper and lower bounds. It is worth noting that the propagation parameters (C^* and m) were not determined for the tested material and were taken from the literature [79]. It means that predictions have a potential for improvement if material based parameters are precisely determined. Moreover, model's predictions remain satisfactory without the consideration of the nature of the critical defect (*i.e.* LoF, corrosion pit or EDM). This provides the possibility of applying the same modelling strategy to other types of defects.

Murakami et al. [24] used a similar method by taking into account the effect of a size dependent threshold in the crack propagation behaviour. Physically, the introduction of this quantity implies that the applied stress is not the absolute driving force of the crack propagation. Murakami et al. underlined that the driving force should be considered as the value of the stress relative to

the fatigue limit. They also observed that the defects were the main reason of the scatter in the fatigue data of a material embedding defects. These observations are in good agreement with the present study.

6. Conclusion

The present study is a contribution towards a better understanding of the 316L L-PBF fatigue behaviour. An experimental campaign was carried out on four specimen batches containing different populations of defects : (i) polished, (ii) pre-corroded, (iii) with an EDM hemispherical defect and (iv) small volume geometry (Fig. 3). The following mains conclusions can be drawn:

1. A large scale of defect size (from 15 μm to 600 μm) was covered using different specimen geometries and introducing corrosion pits and artificial defects.
2. A correlation between the defect size and the fatigue strength of the material was observed. The critical defect's morphology (besides its size) and its nature did not seem to strongly influence the fatigue strength (for pits, LoF pores and EDM artificial defects).
3. The effect of the microstructure was discussed based on a comparison between the L-PBF and wrought materials. Particularly, thanks to small HSV fatigue specimens, the metallic matrix fatigue strength could be estimated. L-PBF material showed fatigue limit two times as high as the wrought one. This may be linked to the higher yield stress of the L-PBF material due to large amount of dislocations related to the material thermal history.
4. Since no effect of the defect's shape was observed, LEFM based models were applied to predict the crack propagation behaviour. Three SIF thresholds models were implemented and identified on the experimental dataset.
5. The use of the Paris law did not allow to obtain satisfactory estimations of the fatigue lives since the dependency of the threshold to the defect size was not taken into account. Then, a modified Paris propagation law using the difference between the SIF ΔK and the SIF crack propagating threshold ΔK_{th} was used in order to model the crack propagation more accurately, particularly, for the short crack regime.
6. The different models applied in this study enabled to globally predict the S–N curves for each defect population based on the knowledge of their size range. The main origin of the scatter observed in the S–N curve (see Fig. 1) was found to be linked to the presence of defects of different sizes. Nevertheless, the results dispersion is not fully understood as many factors may impact the fatigue strength of the material (grain size and morphology, texture, residual stress, ...).

To model the stochastic behaviour linked to microstructural heterogeneities, future work could focus on the definition of a probabilistic framework to increase the quality of the fatigue behaviour predictions.

CRediT authorship contribution statement

Pierre Merot: Writing – review & editing, Writing – original draft, Visualization, Methodology, Investigation, Formal analysis, Data curation, Conceptualization. **Franck Morel:** Writing – review & editing, Validation, Supervision, Project administration, Methodology, Formal analysis, Conceptualization. **Etienne Pessard:** Writing – review & editing, Validation, Supervision, Methodology, Formal analysis, Conceptualization. **Linamaria Gallegos Mayorga:** Writing – review & editing, Validation, Supervision, Methodology, Formal analysis, Conceptualization. **Paul Buttin:** Writing – review & editing, Validation, Supervision, Project administration, Methodology, Formal analysis, Conceptualization. **Thierry Baffie:** Writing – review & editing, Validation, Supervision, Methodology, Formal analysis, Conceptualization.

Declaration of competing interest

The authors declare that they have no known competing financial interests or personal relationships that could have appeared to influence the work reported in this paper.

Data availability

Data will be made available on request.

Acknowledgements

This research was funded by a PhD grant from the French region Pays de la Loire. A special thanks is given to our colleagues from the CEA-LITEN/DTNM/SERE/L3M for L-PBF plates manufacturing, and from the Arts & Métiers institute of technology (Angers) for specimens and experimental set-up machining.

References

[1] DebRoy T, Wei H, Zuback J, Mukherjee T, Elmer J, Milewski J, Beese A, Wilson-Heid A, De A, Zhang W. Additive manufacturing of metallic components - Process, structure and properties. Prog Mater Sci 2018;92:112–224. http://dx.doi.org/10.1016/j.pmatsci.2017.10.001.

[2] Kong D, Dong C, Wei S, Ni X, Zhang L, Li R, Wang L, Man C, Li X. About metastable cellular structure in additively manufactured austenitic stainless steels. Addit Manuf 2021;38:101804. http://dx.doi.org/10.1016/j.addma.2020.101804.

[3] Pace M, Guarnaccio A, Dolce P, Mollica D, Parisi G, Lettino A, Medici L, Summa V, Ciancio R, Santagata A. 3D additive manufactured 316L components microstructural features and changes induced by working life cycles. Appl Surf Sci 2017;418:437–45. http://dx.doi.org/10.1016/j.apsusc.2017.01.308.

[4] Gorsse S, Hutchinson C, Gouné M, Banerjee R. Additive manufacturing of metals: A brief review of the characteristic microstructures and properties of steels, Ti-6Al-4V and high-entropy alloys. Sci Technol Adv Mater 2017;18(1):584–610. http://dx.doi.org/10.1080/14686996.2017.1361305.

[5] Sanaei N, Fatemi A. Defect-based fatigue life prediction of L-PBF additive manufactured metals. Eng Fract Mech 2021;244:107541. http://dx.doi.org/10.1016/j.engfracmech.2021.107541.

[6] Zerbst U, Bruno G, Buffière J-Y, Wegener T, Niendorf T, Wu T, Zhang X, Kashaev N, Meneghetti G, Hrabe N, Madia M, Werner T, Hilgenberg K, Koukolíková M, Procházka R, Džugan J, Möller B, Beretta S, Evans A, Wagener R, Schnabel K. Damage tolerant design of additively manufactured metallic components subjected to cyclic loading: State of the art and challenges. Prog Mater Sci 2021;100786. http://dx.doi.org/10.1016/j.pmatsci.2021.100786.

[7] AlMangour B, Grzesiak D, Borkar T, Yang J-M. Densification behavior, microstructural evolution, and mechanical properties of TiC/316L stainless steel nanocomposites fabricated by selective laser melting. Mater Des 2018;138:119–28. http://dx.doi.org/10.1016/j.matdes.2017.10.039.

[8] Bang GB, Kim WR, Kim HK, Park H-K, Kim GH, Hyun S-K, Kwon O, Kim HG. Effect of process parameters for selective laser melting with SUS316L on mechanical and microstructural properties with variation in chemical composition. Mater Des 2021;197:109221. http://dx.doi.org/10.1016/j.matdes.2020.109221.

[9] Röttger A, Geenen K, Windmann M, Binner F, Theisen W. Comparison of microstructure and mechanical properties of 316 L austenitic steel processed by selective laser melting with hot-isostatic pressed and cast material. Mater Sci Eng A 2016;678:365–76. http://dx.doi.org/10.1016/j.msea.2016.10.012.

[10] Andreau O, Koutiri I, Peyre P, Penot J-D, Saintier N, Pessard E, De Terris T, Dupuy C, Baudin T. Texture control of 316L parts by modulation of the melt pool morphology in selective laser melting. J Mater Process Technol 2019;264:21–31. http://dx.doi.org/10.1016/j.jmatprotec.2018.08.049.

[11] Pham M-S, Dovgyy B, Hooper PA, Gourlay CM, Piglione A. The role of side-branching in microstructure development in laser powder-bed fusion. Nature Commun 2020;11(1):749. http://dx.doi.org/10.1038/s41467-020-14453-3.

[12] Uddin MJ, Ramirez-Cedillo E, Mirshams RA, Siller HR. Nanoindentation and electron backscatter diffraction mapping in laser powder bed fusion of stainless steel 316L. Mater Charact 2021;174:111047. http://dx.doi.org/10.1016/j.matchar.2021.111047.

[13] Gnanasekaran B, Song J, Vasudevan V, Fu Y. Corrosion Fatigue Characteristics of 316L Stainless Steel Fabricated by Laser Powder Bed Fusion. Metals 2021;11(7):1046. http://dx.doi.org/10.3390/met11071046.

[14] Lodhi M, Deen K, Haider W. Corrosion behavior of additively manufactured 316L stainless steel in acidic media. Materialia 2018;2:111–21. http://dx.doi.org/10.1016/j.mtla.2018.06.015.

[15] Bertsch K, Meric de Bellefon G, Kuehl B, Thoma D. Origin of dislocation structures in an additively manufactured austenitic stainless steel 316L. Acta Mater 2020;199:19–33. http://dx.doi.org/10.1016/j.actamat.2020.07.063.

[16] Afkhami S, Dabiri M, Piili H, Björk T. Effects of manufacturing parameters and mechanical post-processing on stainless steel 316L processed by laser powder bed fusion. Mater Sci Eng A 2021;802:140660. http://dx.doi.org/10.1016/j.msea.2020.140660.

[17] Ghayoor M, Lee K, He Y, Chang C-h, Paul BK, Pasebani S. Selective laser melting of 304L stainless steel: Role of volumetric energy density on the microstructure, texture and mechanical properties. Addit Manuf 2020;32:101011. http://dx.doi.org/10.1016/j.addma.2019.101011.

[18] El Khoukhi D, Morel F, Saintier N, Bellett D, Osmond P, Le V-D, Adrien J. Experimental investigation of the size effect in high cycle fatigue: Role of the defect population in cast aluminium alloys. Int J Fatigue 2019;129:105222. http://dx.doi.org/10.1016/j.ijfatigue.2019.105222.

[19] El Khoukhi D, Morel F, Saintier N, Bellett D, Osmond P, Le V-D. Probabilistic modeling of the size effect and scatter in High Cycle Fatigue using a Monte-Carlo approach: Role of the defect population in cast aluminum alloys. Int J Fatigue 2021;147:106177. http://dx.doi.org/10.1016/j.ijfatigue.2021.106177.

[20] Le V-D, Pessard E, Morel F, Edy F. Influence of porosity on the fatigue behaviour of additively fabricated TA6V alloys. In: Hénaff G, editor. MATEC Web Conf 2018;165:02008. http://dx.doi.org/10.1051/matecconf/201816502008.

[21] Blinn B, Klein M, Gläßner C, Smaga M, Aurich J, Beck T. An Investigation of the Microstructure and Fatigue Behavior of Additively Manufactured AISI 316L Stainless Steel with Regard to the Influence of Heat Treatment. Metals 2018;8(4):220. http://dx.doi.org/10.3390/met8040220.

[22] Yadollahi A, Shamsaei N. Additive manufacturing of fatigue resistant materials: Challenges and opportunities. Int J Fatigue 2017;98:14–31. http://dx.doi.org/10.1016/j.ijfatigue.2017.01.001.

[23] Zhang M, Sun C-N, Zhang X, Goh PC, Wei J, Li H, Hardacre D. Competing influence of porosity and microstructure on the fatigue property of laser powder bed fusion stainless steel 316L. In: Solid freeform fabrication 2017: proceedings of the 28th annual international conference. 2017, p. 12.

[24] Murakami Y, Takagi T, Wada K, Matsunaga H. Essential structure of S-N curve: Prediction of fatigue life and fatigue limit of defective materials and nature of scatter. Int J Fatigue 2021;146:106138. http://dx.doi.org/10.1016/j.ijfatigue.2020.106138.

[25] Pessard E, Lavialle M, Laheurte P, Didier P, Brochu M. High-cycle fatigue behavior of a laser powder bed fusion additive manufactured Ti-6Al-4V titanium: Effect of pores and tested volume size. Int J Fatigue 2021;149:106206. http://dx.doi.org/10.1016/j.ijfatigue.2021.106206.

[26] Liang X. High cycle fatigue behavior of additive manufactured stainless steel 316L: Free surface effect and microstructural heterogeneity (Ph.D. thesis), École Nationale Supérieure d'Arts et Métiers; 2020.

[27] Shamir M, Syed AK, Janik V, Biswal R, Zhang X. The role of microstructure and local crystallographic orientation near porosity defects on the high cycle fatigue life of an additive manufactured Ti-6Al-4V. Mater Charact 2020;169:110576. http://dx.doi.org/10.1016/j.matchar.2020.110576.

[28] Le V-D, Saintier N, Morel F, Bellett D, Osmond P. Investigation of the effect of porosity on the high cycle fatigue behaviour of cast Al-Si alloy by X-ray micro-tomography. Int J Fatigue 2018;106:24–37. http://dx.doi.org/10.1016/j.ijfatigue.2017.09.012.

[29] Solberg K, Guan S, Razavi SMJ, Welo T, Chan KC, Berto F. Fatigue of additively manufactured 316L stainless steel: The influence of porosity and surface roughness. Fatigue Fract Eng Mater Struct 2019;ffe.13077. http://dx.doi.org/10.1111/ffe.13077.

[30] Merot P, Morel F, Gallegos Mayorga L, Pessard E, Buttin P, Baffie T. Observations on the influence of process and corrosion related defects on the fatigue strength of 316L stainless steel manufactured by Laser Powder Bed Fusion (L-PBF). Int J Fatigue 2021;155:106552. http://dx.doi.org/10.1016/j.ijfatigue.2021.106552.

[31] Molina CA, Chapetti MD. Estimation of high cycle fatigue behaviour using a threshold curve concept. Int J Fatigue 2018;108:47–52. http://dx.doi.org/10.1016/j.ijfatigue.2017.11.007.

[32] Schijve J. Fatigue of structures and materials. second ed.. Dordrecht: Springer; 2009.

[33] Zhang M, Sun C-N, Zhang X, Goh PC, Wei J, Hardacre D, Li H. Fatigue and fracture behaviour of laser powder bed fusion stainless steel 316L: Influence of processing parameters. Mater Sci Eng A 2017;703:251–61. http://dx.doi.org/10.1016/j.msea.2017.07.071.

[34] Tokaji K, Ogawa T, Harada Y. The growth of small fatigue cracks in a low carbon steel; the effect of microstructure and limitations of linear elastic fracture mechanics. Fatigue Fract Eng Mater Struct 1986;9(3):205–17. http://dx.doi.org/10.1111/j.1460-2695.1986.tb00447.x.

[35] Chapetti MD. Fatigue propagation threshold of short cracks under constant amplitude loading. Int J Fatigue 2003;25(12):8. http://dx.doi.org/10.1016/S0142-1123(03)00065-3.

[36] Pessard E, Bellett D, Morel F, Koutiri I. A mechanistic approach to the Kitagawa-Takahashi diagram using a multiaxial probabilistic framework. Eng Fract Mech 2013;109:89–104. http://dx.doi.org/10.1016/j.engfracmech.2013.06.001.

[37] Chapetti MD. Fatigue assessment using an integrated threshold curve method – applications. Crit Distance Theories Fract 2008;75(7):1854–63. http://dx.doi.org/10.1016/j.engfracmech.2006.11.005.

[38] Garb C, Leitner M, Stauder B, Schnubel D, Grün F. Application of modified Kitagawa-Takahashi diagram for fatigue strength assessment of cast Al-Si-Cu alloys. Int J Fatigue 2018;111:256–68. http://dx.doi.org/10.1016/j.ijfatigue.2018.01.030.

[39] Nadot Y, Nadot-Martin C, Dragon A, Vincent M. Competition between surface defect and grain size under fatigue loading - ARMCO iron. Procedia Struct Integr 2017;7:530–5. http://dx.doi.org/10.1016/j.prostr.2017.11.122.

[40] McEvily A, Minakawa K. Crack closure and the growth of short and long fatigue cracks. Scr Metall 1984;18(1):71–6. http://dx.doi.org/10.1016/0036-9748(84)90092-9.

[41] Sheridan L. A modified El-Haddad model for versatile defect tolerant design. Int J Fatigue 2021;145:106062. http://dx.doi.org/10.1016/j.ijfatigue.2020.106062.

[42] Maierhofer J, Gänser H-P, Pippan R. Modified Kitagawa–Takahashi diagram accounting for finite notch depths. Int J Fatigue 2015;70:503–9. http://dx.doi.org/10.1016/j.ijfatigue.2014.07.007.

[43] Murakami Y. Metal fatigue : effects of small defects and nonmetallic inclusions. Elsevier; 2019, http://dx.doi.org/10.1016/C2016-0-05272-5.

[44] Newman J, Phillips E, Swain M. Fatigue-life prediction methodology using small-crack theory. Int J Fatigue 1999;21(2):109–19. http://dx.doi.org/10.1016/S0142-1123(98)00058-9.

[45] Morel F, Palin-Luc T. A non-local theory applied to high cycle multiaxial fatigue: A non-local theory in multiaxial fatigue. Fatigue Fract Eng Mater Struct 2002;25(7):649–65. http://dx.doi.org/10.1046/j.1460-2695.2002.00527.x.

[46] Nadot, Mendez, Ranganathan, Beranger. Fatigue life assessment of nodular cast iron containing casting defects. Fatigue Fract Eng Mater Struct 1999;22(4):289–300. http://dx.doi.org/10.1046/j.1460-2695.1999.00162.x.

[47] Taylor D. Geometrical effects in fatigue: A unifying theoretical model. Int J Fatigue 1999;21:413–20.

[48] Thieulot-Laure E, Pommier S, Frechinet S. A multiaxial fatigue failure criterion considering the effects of the defects. Int J Fatigue 2007;29(9–11):1996–2004. http://dx.doi.org/10.1016/j.ijfatigue.2007.01.017.

[49] El Haddad M, Topper T, Smith K. Prediction of non propagating cracks. Eng Fract Mech 1979;11(3):573–84. http://dx.doi.org/10.1016/0013-7944(79)90081-X.

[50] Maierhofer J, Pippan R, Gänser H-P. Modified NASGRO equation for physically short cracks. Int J Fatigue 2014;59:200–7. http://dx.doi.org/10.1016/j.ijfatigue.2013.08.019.

[51] Tanaka K, Akiniwa Y. Resistance-curve method for predicting propagation threshold of short fatigue crack at notches. Eng Fract Mech 1988;30(6):863–76. http://dx.doi.org/10.1016/0013-7944(88)90146-4.

[52] Le V-D, Pessard E, Morel F, Prigent S. Fatigue behaviour of additively manufactured Ti-6Al-4V alloy: The role of defects on scatter and statistical size effect. Int J Fatigue 2020;140:105811. http://dx.doi.org/10.1016/j.ijfatigue.2020.105811.

[53] Abroug F, Pessard E, Germain G, Morel F. HCF of AA7050 alloy containing surface defects: Study of the statistical size effect. Int J Fatigue 2018;110:81–94. http://dx.doi.org/10.1016/j.ijfatigue.2018.01.012.

[54] Guerchais R. Influence d'accidents géométriques et du mode de chargement sur le comportement en fatigue à grand nombre de cycles d'un acier inoxydable austénitique 316L (Ph.D. thesis), École Nationale Supérieure d'Arts et Métiers; 2014.

[55] Nadammal N, Cabeza S, Mishurova T, Thiede T, Kromm A, Seyfert C, Farahbod L, Haberland C, Schneider JA, Portella PD, Bruno G. Effect of hatch length on the development of microstructure, texture and residual stresses in selective laser melted superalloy Inconel 718. Mater Des 2017;134:139–50. http://dx.doi.org/10.1016/j.matdes.2017.08.049.

[56] Thijs L, Kempen K, Kruth J-P, Van Humbeeck J. Fine-structured aluminium products with controllable texture by selective laser melting of pre-alloyed AlSi10Mg powder. Acta Mater 2013;61(5):1809–19. http://dx.doi.org/10.1016/j.actamat.2012.11.052.

[57] Bayat M, Mohanty S, Hattel JH. Thermo-fluid-metallurgical modelling of laser-based powder bed fusion process. In: Proceedings of the 2018 COMSOL conference in lausanne. 2018, p. 7.

[58] Andreatta F, Lanzutti A, Vaglio E, Totis G, Sortino M, Fedrizzi L. Corrosion behaviour of 316L stainless steel manufactured by selective laser melting. Mater Corros 2019. http://dx.doi.org/10.1002/maco.201910792.

[59] Wang YM, Voisin T, McKeown JT, Ye J, Calta NP, Li Z, Zeng Z, Zhang Y, Chen W, Roehling TT, Ott RT, Santala MK, Depond PJ, Matthews MJ, Hamza AV, Zhu T. Additively manufactured hierarchical stainless steels with high strength and ductility. Nature Mater 2017;17(1):63–71. http://dx.doi.org/10.1038/nmat5021.

[60] Bajaj P, Hariharan A, Kini A, Kürnsteiner P, Raabe D, Jägle E. Steels in additive manufacturing: A review of their microstructure and properties. Mater Sci Eng A 2020;772:138633. http://dx.doi.org/10.1016/j.msea.2019.138633.

[61] Kong D, Ni X, Dong C, Zhang L, Man C, Yao J, Xiao K, Li X. Heat treatment effect on the microstructure and corrosion behavior of 316L stainless steel fabricated by selective laser melting for proton exchange membrane fuel cells. Electrochim Acta 2018;276:293–303. http://dx.doi.org/10.1016/j.electacta.2018.04.188.

[62] Tucho WM, Lysne VH, Austbø H, Sjolyst-Kverneland A, Hansen V. Investigation of effects of process parameters on microstructure and hardness of SLM manufactured SS316L. J Alloys Compd 2018;740:910–25. http://dx.doi.org/10.1016/j.jallcom.2018.01.098.

[63] Yan F, Xiong W, Faierson E, Olson GB. Characterization of nano-scale oxides in austenitic stainless steel processed by powder bed fusion. Scr Mater 2018;155:104–8. http://dx.doi.org/10.1016/j.scriptamat.2018.06.011.

[64] Andreau O. Nocivité en fatigue et contrôle de défauts produits par fabrication additive (Ph.D. thesis), 2020.

[65] Sun S-H, Ishimoto T, Hagihara K, Tsutsumi Y, Hanawa T, Nakano T. Excellent mechanical and corrosion properties of austenitic stainless steel with a unique crystallographic lamellar microstructure via selective laser melting. Scr Mater 2019;159:89–93. http://dx.doi.org/10.1016/j.scriptamat.2018.09.017.

[66] Hlinka J, Kraus M, Hajnys J, Pagac M, Petrů J, Brytan Z, Tański T. Complex Corrosion Properties of AISI 316L Steel Prepared by 3D Printing Technology for Possible Implant Applications. Materials 2020;13(7):1527. http://dx.doi.org/10.3390/ma13071527.

[67] Maxwell D, Nicholas T. A Rapid Method for Generation of a Haigh Diagram for High Cycle Fatigue. In: Panontin T, Sheppard S, editors. Fatigue and fracture mechanics: 29th volume. West Conshohocken, PA: ASTM International; 1999, p. 626–41. http://dx.doi.org/10.1520/STP14974S.

[68] Merot P, Gallegos Mayorga L, Morel F, Pessard E, Buttin P, Baffie T. 316L L-PBF fatigue dataset. 2022, http://dx.doi.org/10.5281/ZENODO.6653186.

[69] Murakami Y, Endo M. Effects of defects, inclusions and inhomogeneities on fatigue strength. Int J Fatigue 1994;16(3):163–82. http://dx.doi.org/10.1016/0142-1123(94)90001-9.

[70] Bergant M, Werner T, Madia M, Yawny A, Zerbst U. Short crack propagation analysis and fatigue strength assessment of additively manufactured materials: An application to AISI 316L. Int J Fatigue 2021;151:106396. http://dx.doi.org/10.1016/j.ijfatigue.2021.106396.

[71] Schönbauer BM, Mayer H. Effect of small defects on the fatigue strength of martensitic stainless steels. Int J Fatigue 2019;127:362–75. http://dx.doi.org/10.1016/j.ijfatigue.2019.06.021.

[72] Kitagawa H, Takahashi S. Applicability of fracture mechanics to very small cracks or the cracks in the early stage. In: Second international conference on mechanical behavior of materials. 1976, p. 627–31.
[73] Chapetti MD. A simple model to predict the very high cycle fatigue resistance of steels. Int J Fatigue 2011;33(7):833–41. http://dx.doi.org/10.1016/j.ijfatigue.2010.12.010.
[74] Riemer A, Richard HA. Crack Propagation in Additive Manufactured Materials and Structures. Procedia Struct Integr 2016;2:1229–36. http://dx.doi.org/10.1016/j.prostr.2016.06.157.
[75] Maierhofer J, Kolitsch S, Pippan R, Gänser H-P, Madia M, Zerbst U. The cyclic R-curve – Determination, problems, limitations and application. Eng Fract Mech 2018;198:45–64. http://dx.doi.org/10.1016/j.engfracmech.2017.09.032.
[76] Rokhlin SI. Effect of pitting corrosion on fatigue crack initiation and fatigue life. Eng Fract Mech 1999;20.
[77] Gerberich WW, Harvey SE, Kramer DE, Hoehn JW. Low and high cycle fatigue - A continuum supported by AFM observations. Acta Metall 1998;46(14):15.
[78] Xiulin Z, Hirt MA. Fatigue crack propagation in steels. Eng Fract Mech 1983;18(5):965–73. http://dx.doi.org/10.1016/0013-7944(83)90070-X.
[79] Riemer A, Leuders S, Thöne M, Richard H, Tröster T, Niendorf T. On the fatigue crack growth behavior in 316L stainless steel manufactured by selective laser melting. Eng Fract Mech 2014;120:15–25. http://dx.doi.org/10.1016/j.engfracmech.2014.03.008.
[80] Calderon-Uriszar-Aldaca I, Briz E, Biezma M, Puente I. A plain linear rule for fatigue analysis under natural loading considering the coupled fatigue and corrosion effect. Int J Fatigue 2019;122:141–51. http://dx.doi.org/10.1016/j.ijfatigue.2019.01.008.
[81] Li S-X, Akid R. Corrosion fatigue life prediction of a steel shaft material in seawater. Eng Fail Anal 2013;34:324–34. http://dx.doi.org/10.1016/j.engfailanal.2013.08.004.